Mechanism and Kinetic Isotope Effect of the Reaction of $C_2(X^1\Sigma_g^+)$ Radicals with H_2 and D_2

Masakazu Nakajima, Akira Matsugi, and Akira Miyoshi*

Department of Chemical System Engineering, School of Engineering, University of Tokyo, 7-3-1 Hongo, Bunkyo-ku, Tokyo 113-8656, Japan

Received: May 5, 2009; Revised Manuscript Received: June 23, 2009

The rate constants for the reactions of $C_2(X^1\Sigma_g^+)$ with H_2 and D_2 have been investigated experimentally and theoretically to assess the statistical theory of the reaction and to reveal the mechanism of the reaction. The ground-state C_2 radicals were generated by multiphoton laser-photolysis of C_2Cl_4 at 248 nm and were probed by a laser-induced fluorescence method using the Mulliken system ($D^1\Sigma_u^+-X^1\Sigma_g^+$). Rate constants have been measured to be $k[C_2(X)+H_2] = 5.6 \times 10^{-11}$ exp[−9.1 (kJ mol^{-1})/*RT*] and $k[C_2(X)+D_2] = 3.2 \times 10^{-11}$ exp[−9.9 (kJ mol^{-1})/*RT*] cm^3 molecule^{-1} s^{-1} in the temperature range 293−395 K and at total pressure around 10 Torr (He buffer). Quantum chemical calculations at the MRCI level revealed that the reaction predominantly proceeds via a collinear direct-abstraction transition state. The measured rate constants as well as the kinetic isotope effect were well reproduced by the transition-state theory based on the MRCISD+Q/aug-cc-pV5Z calculations, provided that the anharmonic bending vibrations of the transition states were properly treated. The effect of the Davidson correction was found to be significant for the potential energy surface around the early transition state.

Introduction

Dicarbon (C_2) is one of the simplest transient molecules, and it has been observed in astronomical objects[1−3] and hydrocarbon flames[4,5] via the strong transitions of the Swan system ($d^3\Pi_g-a^3\Pi_u$). Its lowest electronic excited state, $a^3\Pi_u$, lies above the ground state, $X^1\Sigma_g^+$, by only 610 cm^{-1} as a difference of zero vibrational levels. Previous kinetic studies[6−23] showed that $C_2(X^1\Sigma_g^+)$ is more reactive than $C_2(a^3\Pi_u)$ toward most of the reactants. This is true for reactions with H_2; higher activation energy has been reported for the a-state (25.0 kJ mol^{-1})[14] than for the singlet ground state (12.2 kJ mol^{-1}).[15] The reaction of $C_2(a)$ with H_2 has been believed to be a direct hydrogen abstraction reaction,[14] while that of $C_2(X)$ has been speculated to be an insertion reaction[15] by analogy with the reactions of $O(^1D)$. Theoretical investigations have also supported the mechanism of $C_2(a) + H_2$.[20,23] In the only previous theoretical study on $C_2(X) + H_2$, to the authors' knowledge, MP2 calculations with a restricted Hartree−Fock (RHF) wave function showed a T-shaped transition state leading to the formation of vinylidene (:C═CH_2).[24] However, the predicted barrier height (42.3 kJ mol^{-1}) was significantly higher than the experimental activation energy (12.2 kJ mol^{-1}). The RHF wave function is insufficient for the description of the electronic state of $C_2(X)$ which should have, at least in part, the biradical nature of a Lewis structure ·C≡C·.[25] Here, it is interesting to state that $C_2(X)$ is a singlet biradical of a type different from $O(^1D)$, $NH(a^1\Delta)$, and $CH_2(^1A_1)$, all of which are biradicals at one center (namely, :O, :NH and :CH_2), and the reaction of $C_2(X)$ is not necessarily similar to that for these one-centered biradicals. In this sense, it is of further interest to reveal the mechanism of $C_2(X) + H_2$ that is not categorized in the well-known types of reactions.

The H/D kinetic isotope effect is a well-known and powerful tool for the elucidation of the mechanism for reactions involving hydrogen atoms.[26] Although the rate constants have been reported for the reactions of $C_2(a)$ with H_2 and D_2,[14] no measurement for $C_2(X) + D_2$ has been reported. Measurements of the kinetic isotope effect for $C_2(X) + H_2/D_2$ will be useful for understanding the mechanism of this reaction. Another point of interest for the measurement of the kinetic isotope effect is that it can be a touchstone for the statistical theory of the reactions. In many previous kinetic studies, transition-state theory (TST) analyses were generally successful. This is probably because there is no significant flaw in the theory, but also because there are usually several adjustable parameters, especially the height of the barrier. Even with the high accuracy quantum chemical methods, such as G3[27] and CBS-QB3,[28] the mean absolute error is reported to be 4−5 kJ mol^{-1}. If this value is directly applied for the barrier height, a change of the rate constants of more than ± 5 times is allowed at ∼300 K. To reduce such an ambiguity, one can compare theory with experimental rate constant over a wide temperature range.[29] Further clarification can be achieved by comparing the experimentally determined isotopic rate constants with theoretical values. Since the potential energy surface is the same for isotopic reactions (under the Born−Oppenheimer approximation), the adjustment of the potential barrier, even if it is needed, must be exactly the same for all isotopic reactions. An additional advantage of the kinetic isotope effect for testing theory is that the possible systematic errors in experiments are expected to be canceled in the ratio of the isotopic rate constants by measuring them in the same experimental system.

In the present study, rate constants for $C_2(X) + H_2$ and D_2 have been determined in the temperature range 293−395 K by using the pulsed-laser photolysis/laser-induced fluorescence (PLP/LIF) technique via the Mulliken system of C_2 ($D^1\Sigma_u^+-X^1\Sigma_g^+$). The results were compared with the theo-

* To whom correspondence should be addressed. E-mail: miyoshi@chemsys.t.u-tokyo.ac.jp.

10.1021/jp904165s CCC: $40.75
Published on Web 07/14/2009

retical rate constants based on the multireference configuration interaction (MRCI) potential energy calculations.

Experimental Section

LIF According to the Mulliken System. In most of the previous kinetic studies,[9−12,15] the Phillips system ($A^1\Pi_u-X^1\Sigma_g^+$) had been used for the LIF measurement of $C_2(X)$. However, due to the long radiative lifetime of the $A^1\Pi_u$ state (10.7 μs for $v = 4$),[30] these experiments often suffered from the low fluorescence quantum yield due to collisional quenching. In addition, quantum efficiency of a photomultiplier tube (PMT) is low for the A → X fluorescence in the near-infrared region ($T_{4-1} = 12\,632$ cm^{-1} for the 4−1 band).[31] In this study, instead of the Phillips system, the Mulliken system ($D^1\Sigma_u^+-X^1\Sigma_g^+$) was adopted for the detection of $C_2(X)$. The transition is located in the UV region where the sensitivity of a PMT is high, and the radiative lifetime of the $D^1\Sigma_u^+$ state is much shorter ($\tau_f \sim 18$ ns for $v = 0$)[32] than that of the A state. One possible disadvantage in employing the Mulliken system is that the $\Delta v = 0$ transitions are dominant,[33] and the fluorescence cannot be separated from the scattering or the stray light of the probe laser by an optical filter. Neither is temporal distinction of the fluorescence from the scattered probe light due to the short lifetime of the $D^1\Sigma_u^+$ state. However, these disadvantages could easily be compensated for by the large oscillator strength of the Mulliken system. A very small intensity of the probe laser was enough to obtain a sufficient amount of fluorescence, and the fluorescence could be detected almost free from scattering.

Generation of $C_2(X)$. An ordinary PLP/LIF apparatus was used in the present study. The multiphoton dissociation of tetrachloroethylene, C_2Cl_4, was used as a source of $C_2(X)$. Liquid C_2Cl_4 (Sigma-Aldrich, 99.9%) was degassed by freeze−pump−thaw cycles and was used without further purification. The liquid precursor was bubbled with He, and the gas containing C_2Cl_4 was introduced to the reaction cell with inner diameter of 43 mm. The partial pressure of C_2Cl_4 in the gas was estimated from its vapor pressure (18 Torr) at 298 K. The concentration of C_2Cl_4 in the reaction cell was kept around 2×10^{13} molecules cm^{-3} under typical conditions. Light at 248 nm from a pulsed KrF excimer laser (Lambda Physik, Compex 102) irradiated the sample gas perpendicularly to the gas-flow direction. The 248 nm light with typical pulse energy ≈30 mJ cm^{-2} was loosely focused by a $f = 200$ mm convex lens to attain fluence of ≈330 mJ cm^{-2} required for multiphoton dissociation of C_2Cl_4 in the observation region.

Experimental Procedures. A dye laser (Lambda Physik, ScanMate) pumped by a pulsed XeCl excimer laser (Lambda Physik, Compex 102) was used as a probe laser. The output of the dye laser was doubled by a BBO (β-barium borate) crystal to obtain around 230 nm output and introduced to the reaction cell collinear with and counterpropagating to the photolysis laser beam through a window attached to the cell at Brewster's angle. The timing and repetition rate of the photolysis and probe lasers were controlled by a homemade pulse generator. The wavelength of the probe laser was tuned to the $R(8)$ line of the origin band of the Mulliken system (231.158 nm) for LIF detection of $C_2(X)$. The 0−0 band fluorescence was monitored through an interference filter (center wavelength 228 nm, fwhm 10 nm) with a PMT (Hamamatsu, R928). Signal from the PMT was amplified with a 350 MHz preamplifier (Stanford research, SR-240A), and accumulated by a gated integrator (Stanford Research, SR250). The integrated signal was transferred to a personal computer via a computer interface module (Stanford research, SR245). Temporal decay profiles of the $C_2(X)$ concentration were recorded at several concentrations of the reactant H_2 or D_2 in the range $(0.5-4.5) \times 10^{16}$ molecules cm^{-3}. The total pressure in the reaction cell was monitored by a capacitance manometer (MKS, Baratron 622A; full scale 100 Torr).

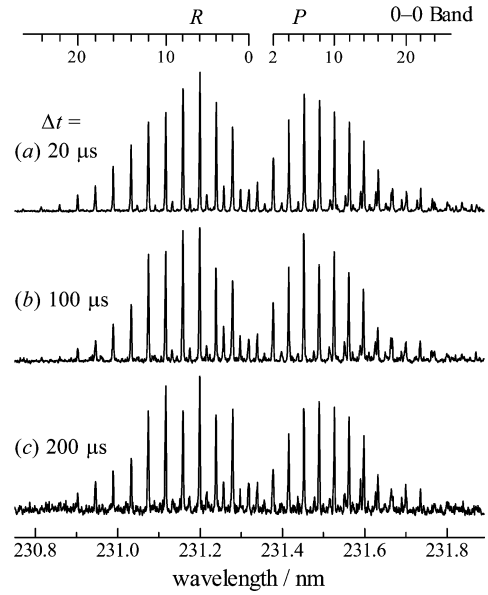

Figure 1. LIF excitation spectra of the C_2 Mulliken system, $D^1\Sigma_u^+-X^1\Sigma_g^+$, in $\Delta v = 0$ region at different photolysis-probe delay times, $\Delta t =$ (a) 10 μs, (b) 100 μs, and (c) 200 μs, under a total pressure of 10.1 Torr (He). Weak rotational lines not assigned to the 0−0 band originate from excited vibrational levels in the X state.

Experimental Results

Two-Photon Dissociation of C_2Cl_4. To confirm the photolysis process of C_2Cl_4 used as a source of $C_2(X)$ radicals, relative concentrations of $C_2(X)$ were measured via LIF as a function of the photolysis-laser pulse energies. The result is shown in Figure 1S (Supporting Information). The slope of the double logarithmic plot of LIF intensity vs photolysis laser energy was 1.97, meaning that $C_2(X)$ was predominantly produced from a two-photon process of C_2Cl_4. From the reaction enthalpy of $C_2Cl_4 \rightarrow C_2(X) + 2\ Cl_2$ (850 kJ mol^{-1})[34] and 248 nm photon energy (corresponding to 482 kJ mol^{-1}), a two-photon process seems to be reasonable for the production of $C_2(X)$.

LIF Spectra and Possible Interferences. Figure 1 shows LIF excitation spectra of the $\Delta v = 0$ sequences of the Mulliken system ($D^1\Sigma_u^+-X^1\Sigma_g^+$) observed under typical experimental conditions. Rotational assignment could be done unambiguously with the reported molecular constants.[33,35] Although the rotational relaxation occurs within ∼10 μs after photolysis, hot bands were recognized with moderate intensities in Figure 1. Since the relative intensities of the hot bands to the 0−0 band were unchanged for 200 μs (Figure 1a−c), the vibrational relaxation was considered to be negligibly slow under the present experimental conditions. Another possible interference to the kinetic measurements is the quenching of $C_2(a)$ to $C_2(X)$, though no experimental evidence for this was observed in the present study. Unfortunately, no measurement was reported for He, but upper limits of the quenching rate constants have been reported to be $<3 \times 10^{-14}$ cm^3 molecule^{-1} s^{-1} for Ar, N_2, CO_2, and CF_4.[12] By taking into account the upper limits for the rates of the overall removal of $C_2(a)$, which includes both reaction and quenching, $<5 \times 10^{-15}$ (H_2)[9] and $<1 \times 10^{-16}$ (CH_4)[8] cm^3 molecule^{-1} s^{-1}, we can estimate the quenching rate constant

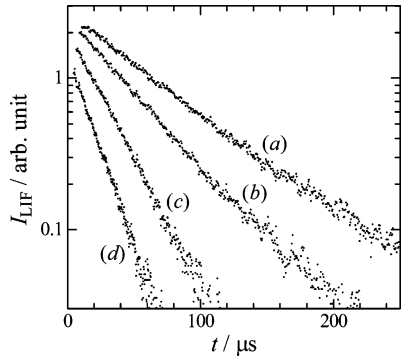

Figure 2. Semilogarithmic plot of the temporal LIF intensity profiles of $C_2(X)$ with (a) $[H_2] = 0.42$, (b) 0.84, (c) 1.70, and (d) 3.33×10^{16} molecules cm^{-3} at 10 Torr total pressure (He buffer) and 295 K.

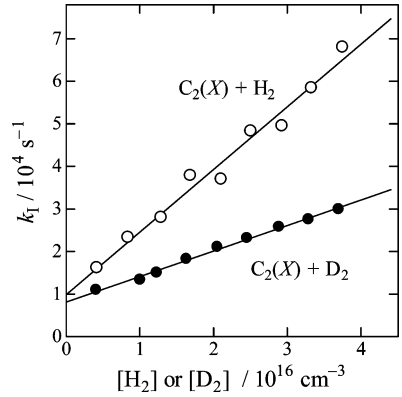

Figure 3. Pseudo-first-order plots of the rate constants for $C_2(X) + H_2$ (open circles) and $C_2(X) + D_2$ (solid circles) reactions at 10 Torr total pressure (He buffer) and at 295 K.

for He to be $<5 \times 10^{-15}$ cm^3 $molecule^{-1}$ s^{-1}. This is too small to interfere with the $C_2(X)$ profiles in the experimental time scale (<200 μs) and under He pressure, 10 Torr or 6.5×10^{17} molecules cm^{-3}. It should be noted that the choice of the opposite extreme condition, that is, the rapid quenching conditions with efficient quencher, is not appropriate considering the large equilibrium constant $K_c = [C_2(a)]/[C_2(X)] \approx 0.35$ at room temperature. It will result in the measurement of 1:0.35 weighted average of $C_2(X)$ and $C_2(a)$ reactions.

Rate Constants and Kinetic Isotope Effect. Although the quantitative estimate is difficult for the two-photon process of C_2Cl_4, the concentration of $C_2(X)$ is estimated to be much smaller (e.g., probably $<10^{-2}$) than that of the precursor ($\sim 2 \times 10^{13}$ molecules cm^{-3}). The total consumption kinetics of $C_2(X)$ should thus be the pseudo-first-order, and it was confirmed that the change of the concentration of C_2Cl_4 did not affect the measured first-order decay. The observed temporal profiles of $[C_2(X)]$ are shown in Figure 2. The pseudo-first-order rate constants are plotted in Figure 3 against the concentration of H_2 or D_2. Slopes of the plots in Figure 3 gave second-order rate coefficients, $k[C_2(X)+H_2] = (1.47 \pm 0.17) \times 10^{-12}$ and $k[C_2(X)+D_2] = (0.600 \pm 0.034) \times 10^{-12}$ cm^3 $molecule^{-1}$ s^{-1} at 295 K and 10 Torr (He), where error limits are two standard deviations derived from the pseudo-first-order analyses. Intercepts of the plots in Figure 3, $\sim 1 \times 10^4$ s^{-1}, correspond to the reaction with the precursor C_2Cl_4 and a loss due to diffusion. The rate coefficient of the $C_2(X) + C_2Cl_4$ has been reported to be 2.6×10^{-10} cm^3 $molecule^{-1}$ s^{-1} (300 K),[12] and its contribution to the intercept is calculated to be 5×10^3 s^{-1} at $[C_2Cl_4] \sim 2 \times 10^{13}$ molecules cm^{-3}. The rate constants determined at total pressures of 5 and 20 Torr are listed in Table 1 with the

TABLE 1: Experimental Conditions and Rate Constants for $C_2(X) + H_2/D_2$

T/K	p^a/ Torr	$[C_2Cl_4]$/ 10^{13} molecules cm^{-3}	$k(H_2)/10^{-12}$ cm^3 $molecule^{-1}$ s^{-1}	$k(D_2)/10^{-12}$ cm^3 $molecule^{-1}$ s^{-1}	$k(H_2)/k(D_2)$
295	5	2.0	1.60 ± 0.28^b	0.618 ± 0.096^b	2.59
295	10	2.0	1.47 ± 0.17	0.600 ± 0.034	2.45
295	20	2.0	1.36 ± 0.15	0.584 ± 0.051	2.33
293	10	1.5	1.44 ± 0.05	0.586 ± 0.027	2.46
324	10	1.3	1.81 ± 0.10	0.762 ± 0.055	2.38
353	10	1.2	2.48 ± 0.18	1.08 ± 0.09	2.30
375	10	1.1	2.93 ± 0.29	1.30 ± 0.08	2.25
395	10	1.1	3.62 ± 0.24	1.60 ± 0.08	2.26

[a] Total pressure was maintained by a He buffer. [b] Indicated error limits are two standard deviations (2σ) derived from the pseudo-first-order analyses.

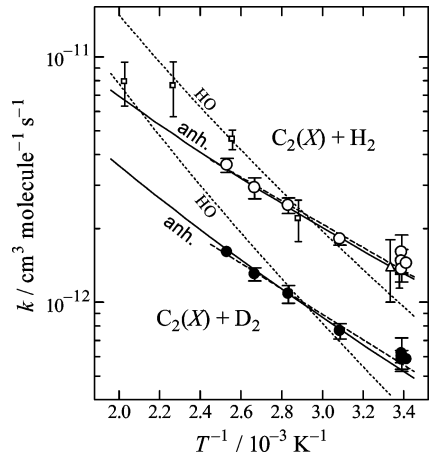

Figure 4. Arrhenius plot of the rate constants for $C_2(X) + H_2$ and $C_2(X) + D_2$. Present experimental results for $C_2(X) + H_2$ and $C_2(X) + D_2$ are shown by open and solid circles, respectively. Previous reports for $C_2(X) + H_2$ are shown by open squares[15] and open triangles.[10] Error bars indicate two standard deviations. Dashed lines represent the results of the Arrhenius fit. Dotted lines (marked with "HO") and solid lines (marked with "anh") denote theoretical rate constants calculated by the harmonic oscillator approximation and those by the anharmonic treatment, respectively. See text for detail.

experimental conditions. No significant pressure dependence was observed. Temperature dependence of the rate constants measured in the range 293−395 K is shown in Figure 4 and Table 1. Rate constants for $C_2(X) + H_2$ agreed well with the previous measurements.[9,12] Isotopic rate constants for $C_2(X) + D_2$ are about 39−44% of that for H_2. A simple Arrhenius fit to the experimental data gave the following expressions for the rate constants for $C_2(X)$ with H_2 and D_2 and are shown by dashed lines in Figure 4.

$$k[C_2(X)+H_2] = 5.6 \times 10^{-11} \exp[-9.1 \text{ (kJ mol}^{-1})/RT] \text{ cm}^3 \text{ molecule}^{-1} \text{ s}^{-1}$$

$$k[C_2(X)+D_2] = 3.2 \times 10^{-11} \exp[-9.9 \text{ (kJ mol}^{-1})/RT] \text{ cm}^3 \text{ molecule}^{-1} \text{ s}^{-1}$$

Theoretical Calculations

Quantum Chemical Calculations. The stationary points for the $C_2(X) + H_2$ reaction were calculated with the internally contracted MRCI method by using the MOLPRO 2002.6 and 2008.1 programs.[36] Wave functions obtained from the preceding full-valence multiconfiguration self-consistent field (MCSCF) calculation were used in the MRCI calculations. Calculations

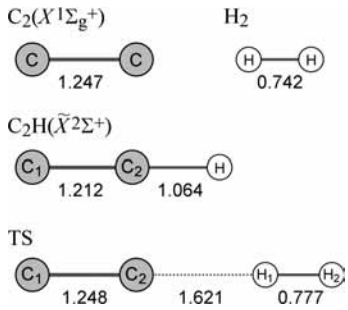

Figure 5. Geometries of $C_2(X)$, H_2, C_2H, and transition state (TS) optimized by the MRCISD+Q/aug-cc-pV5Z method.

with RCCSD(T) method were also done for comparison. Dunning's correlation-consistent basis sets, cc-pVTZ to aug-cc-pV5Z, were used for the geometry optimizations and frequency calculations. By calculating the energies of the reactants and the products at a sufficiently large separation, we confirmed that, with the Davidson correction included, the size inconsistency of the truncated CI energy was reduced to be less than 1 kJ mol^{-1}.

The optimized geometries of the reactants, $C_2(X)$ and H_2, the product, C_2H, and transition state (TS) at the MRCISD+Q/aug-cc-pV5Z level are shown in Figure 5. The geometries and vibrational frequencies calculated at different levels of theory are summarized in Tables 1−3 with experimental geometries and frequencies.[37−39] For $C_2(X)$ and H_2, as shown in Table 2, both of the methods, RCCSD(T) and MRCI, gave nearly identical results, which seem to approach the experimental values at the large basis-set limit. This seems to be true for the results of C_2H shown in Table 3 considering that the experimental values are for the effective geometry and $v = 1-0$ transitions. However, for the transition state, as shown in Table 4, RCCSD(T) and MRCI gave significantly different results. In particular, the RCCSD(T) gave imaginary frequencies for two bending modes of the linear CCHH transition state, implying that the T-shape transition state for insertion reaction is lower on the RCCSD(T) potential energy hypersurface. The IRC (intrinsic reaction coordinate) calculations at the MRCISD/cc-pVQZ level revealed that the calculated TS leads to direct H-atom abstraction, producing C_2H and H. Additionally, a two-dimensional PES (potential energy surface) was calculated at MRCISD/cc-pVQZ level for the collinear approach of $C_2(X)$ to H_2 with a fixed C−C bond length, which is nearly the spectrator and changes little from the reactant to the saddle point. The result is shown in Figure 2S (Supporting Information), which clearly indicates that the collinear approach of $C_2(X)$ to H_2 correlates to the $C_2H + H$ products via an early saddle point. This is different from the insertion mechanism previously suggested, the conclusion for which is based on the experimental activation energy[15] and the RHF calculations.[24] These predicted a planar T-shape (C_{2v}) transition state correlating to the vinylidene ($:C{=}CH_2$). With the MRCI method, the T-shape transition state has two imaginary frequencies and corresponds to the torsion barrier of the transition state as will be discussed later. Since the T-shape TS was found to be above the linear TS by 539 cm^{-1} at the MRCISD+Q/aug-cc-pV5Z level, it was concluded that direct H-atom abstraction via the linear transition state is the dominant channel for this reaction.

Conventional Transition-State Theory (TST). The TS is located in the early part of the IRC as shown in Figure 2S (Supporting Information), and its geometry was found to be close to the reactants, as shown in Table 4. As is often the case for such a loose TS, the optimized geometry, especially the length of the newly forming C−H bond, depends significantly on the size of the basis set. Also, the location of the top of the loose maximum is significantly affected by the inclusion of the Davidson correction, which for this case increased the C_2-H_1 distance by 0.05 Å on the MRCISD+Q potential energy hypersurface compared to the uncorrected one. A significant effect was also seen in the vibrational frequency of the H−H stretching and bending modes, for which a detailed discussion will be given later. The energies calculated at the MRCISD+Q/aug-cc-pV5Z level are summarized in Table 5. The calculated threshold energies, 9.26 and 10.04 kJ mol^{-1} for $C_2(X) + H_2$ and D_2, respectively, correspond with the respective experimental activation energies, 9.1 and 9.9 kJ mol^{-1}. As a starting point, TST rate constants with the rigid rotor (RR) and harmonic oscillator (HO) approximations were calculated by using the geometries and vibrational frequencies calculated at the MRCISD+Q/aug-cc-pV5Z level. The one-dimensional tunneling correction was made by assuming an asymmetric Eckert potential.[40,41] However, the conventional TST calculation could not accurately reproduce the experiments, as shown by the dotted lines in Figure 4. The potential energy barrier was adjusted ($\Delta_{adj}E = +3.3$ kJ mol^{-1}) so that the calculations agree with the experiments in the middle of the temperature range, 340 K. Apparently, the TST calculation overestimates the temperature dependence of the rate constants, or in other words, it overestimates the pre-exponential factor, which results in the unrealistically high barrier for the reproduction of the experimental rate constants. Vibrational frequency calculations at the several geometry along the IRC by the MRCISD/cc-pVQZ method indicated that the variational effect was minor for this reaction.

Anharmonicity of Bending Vibrations of the TS. As was found in the previous study,[29] anharmonicity of the transitional vibrational modes of the TS is often the cause of discrepancies between TST and experimental rate constants. Thus, the potential energy curves along the two degenerate bending coordinates of the TS were calculated by the MRCISD/cc-pVQZ method. Since the normal-mode analysis of CCHH and CCDD transition states indicate that the normal coordinates can be approximated by the internal coordinates, α and β, shown in Figure 6, potential energies were calculated by restricting either of the angles α or β. All the other geometric parameters were relaxed by a saddle-point optimization. The results are shown in Figure 6, and both of the potential energy curves indicate strong anharmonicity. It should be noted that the point $\beta = +90°$ or $-90°$ in Figure 6b corresponds to the T-shape transition state described before and it is a second-order saddle point having two imaginary frequencies. The Davidson correction significantly affects the potential energy hypersurface in the vicinity of the transition state. The correction significantly lowered the energy of the T-shape transition state relative to the linear transition state as shown in Figure 6b. It also affects the shape of the potential energy curve; the bottom part of the potential energy curve along β is significantly flattened by the correction. A similar effect can be seen in the calculation with a larger basis set as shown in Table 4, where the ω_4 at MRCISD+Q/aug-cc-pV5Z (201 cm^{-1}) is significantly smaller than that at MRCISD/aug-cc-pV5Z (266 cm^{-1}). To assess the accuracy of the potential energy curves obtained at a lower level of theory, MRCISD+Q/cc-pVQZ//MRCISD/cc-pVQZ, two second-order saddle points corresponding to $\alpha = 90°$ and $\beta = 90°$ were optimized on the MRCISD+Q/aug-cc-pV5Z energy. The resultant barrier heights along α and β, 7109 and 539 cm^{-1}, respectively, were only slightly smaller than those shown in

TABLE 2: Calculated Geometries and Vibrational Frequencies of $C_2(X)$ and H_2

		$C_2(X^1\Sigma_g^+)$				H_2			
		$r_e(C-C)^a$		$\omega_e(^{12}C_2)^b$		$r_e(H-H)^a$		$\omega_e(^1H_2)^b$	
method	basis set	Å	% ε^c	cm^{-1}	% ε^c	Å	% ε^c	cm^{-1}	% ε^c
RCCSD(T)	cc-pVTZ	1.2507	0.7	1845	−0.5	0.7427	0.2	4409	0.2
	cc-pVQZ	1.2458	0.3	1855	0.0	0.7419	0.1	4403	0.0
MRCISD	cc-pVTZ	1.2520	0.8	1840	−0.8	0.7427	0.2	4409	0.2
	cc-pVQZ	1.2470	0.4	1851	−0.2	0.7419	0.1	4403	0.0
	aug-cc-pVQZ	1.2472	0.4	1856	0.1	0.7420	0.1	4400	0.0
	cc-pV5Z	1.2459	0.3	1854	0.0	0.7416	0.0	4404	0.1
	aug-cc-pV5Z	1.2460	0.3	1856	0.1	0.7416	0.0	4403 [3114]^d	0.0
MRCISD+Q	aug-cc-pV5Z	1.2466	0.3	1850	−0.2				
exp[37]		1.24253		1854.7		0.74144		4401.2	

^{a} Equilibrium nuclear distances. ^{b} Harmonic vibrational frequencies at equilibrium nuclear positions. ^{c} Percentage differences from the experimental values. ^{d} Vibrational frequency of $^2H_2$.

TABLE 3: Calculated Geometries and Vibrational Frequencies of C_2H

		r_e^a/Å		$\omega_e(^{12}C_2{}^1H)^b/cm^{-1}$		
method	basis set	C_1-C_2	C_2-H	ω_1 CH str	ω_2 CC str	ω_3 bend.
RCCSD(T)	cc-pVTZ	1.2150	1.0646	3455	2012	322
	cc-pVQZ	1.2110	1.0645	3446	2021	361
MRCISD	cc-pVTZ	1.2163	1.0644	3452	2002	376
	cc-pVQZ	1.2123	1.0642	3445	2012	408
	aug-cc-pVQZ	1.2125	1.0643	3445	2011	412
	cc-pV5Z	1.2113	1.0639	3446	2015	425
	aug-cc-pV5Z	1.2114	1.0639	3446	2014	424
MRCISD+Q	aug-cc-pV5Z	1.2117	1.0641	3446 [2656]^c	2012 [1884]^c	401 [319]^c
exp[38,39]		(1.2165)^a	(1.0465)^a	(3299)^b	(1841)^b	(372)^b

^{a} Equilibrium nuclear distances. See Figure 5 for numbering of atoms. Experimental values are effective distances. ^{b} Harmonic vibrational frequencies of $^{12}C_2{}^1H$ at equilibrium nuclear positions. Experimental values are those for $v = 1-0$ transitions. ^{c} Values in brackets are vibrational frequencies of $^{12}C_2{}^2H$.

TABLE 4: Calculated Geometries and Vibrational Frequencies of the Transition State

		r_e^a/Å			$\omega_e(^{12}C_2{}^1H_2)^b/cm^{-1}$				
method	basis set	C_1-C_2	C_2-H_1	H_1-H_2	ω_1 HH str	ω_2 CC str	ω_3 rc^c	ω_4 bend.	ω_5 bend.
RCCSD(T)	cc-pVTZ	1.2505	1.6946	0.7678	3744	1858	482 i	123 i	279 i
	cc-pVQZ	1.2460	1.7148	0.7654	3790	1864	449 i	129 i	247 i
MRCISD	cc-pVTZ	1.2525	1.5545	0.7892	3273	1845	547 i	291	137
	cc-pVQZ	1.2478	1.5691	0.7861	3323	1853	541 i	245	133
	aug-cc-pVQZ	1.2481	1.5725	0.7858	3333	1851	534 i	267	140
	cc-pV5Z	1.2468	1.5711	0.7857	3329	1855	534 i	264	143
	aug-cc-pV5Z	1.2469	1.5716	0.7857	3329	1855	534 i	266	143
MRCISD+Q	aug-cc-pV5Z	1.2479	1.6206	0.7773	3519 [2491]^d	1845 [1844]^d	483 i [355 i]^d	201 [157]^d	99 [79]^d

^{a} Equilibrium nuclear distances. See Figure 5 for numbering of atoms. ^{b} Harmonic vibrational frequencies of $^{12}C_2{}^1H_2$ at equilibrium nuclear positions. ^{c} Reaction coordinate. ^{d} Values in brackets are vibrational frequencies of $^{12}C_2{}^2H_2$.

TABLE 5: Energetics for the Reaction of $C_2(X) + H_2$

			$\Delta_{adj}E$/kJ mol^{-1}		E_{0K}(rel)^d/kJ mol^{-1}	
	E(MRCISD+Q/aug-cc-pV5Z)/hartree	E_{pot}(rel)^a/kJ mol^{-1}	HO^b	anh^c	$^{12}C_2-{}^1H_2$	$^{12}C_2-{}^2H_2$
$C_2(X) + H_2$	−76.981732	0			0	0
transition state	−76.977548	10.99	3.3	−1.8	9.26	10.04
$C_2H + H$	−76.995195	−35.35			−35.30	−34.07

^{a} MRCISD+Q potential energy relative to the reactants. ^{b} Potential energy adjustment for the TST fit with harmonic oscillator (HO) approximation. ^{c} Potential energy adjustment for the TST fit with anharmonic (anh) treatment. ^{d} Potential energy relative to the reactants corrected for the zero-point energy by using MRCISD+Q/aug-cc-pV5Z harmonic frequencies.

Figure 6 (7190 and 561 cm^{-1}, respectively). The potential energy curves were used in the later calculations after a small scaling factor was applied to match the MRCISD+Q/aug-cc-pV5Z barrier heights.

TST with Anharmonic Treatment. The vibrational energy levels of these bending modes may be calculated by assuming independent one-dimensional vibration for each of the degenerate coordinates. However, from Figure 6, the classical turning points at 200 cm^{-1} ($\approx kT$ at room temperature) are found around $\alpha = \pm 20°$ and $\beta = \pm 50°$, which are too large for the one-dimensional assumption. Thus, the vibrational eigenstates were calculated by solving the two-dimensional Schrödinger equation. Since the electronic state of the transition state is Σ^+, the potential energy must have cylindrical symmetry. The Schrödinger equation for this problem can be separated into colatitudinal and azimuthal parts, and the colatitudinal part was solved

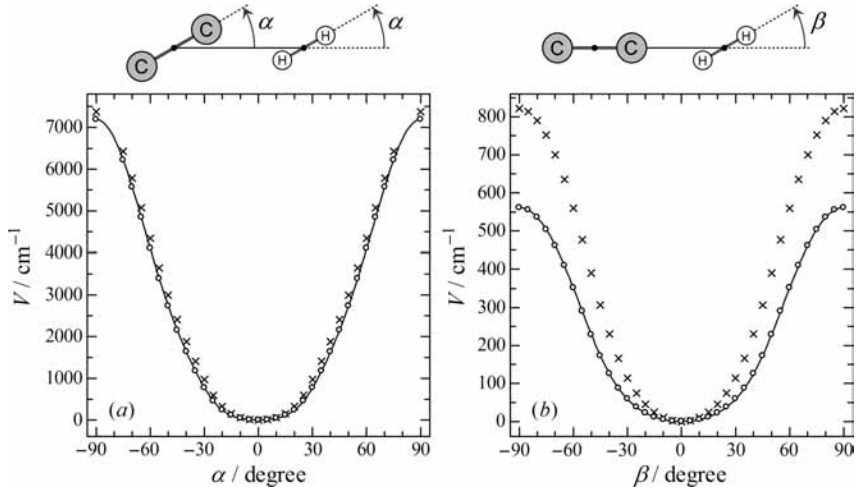

Figure 6. Potential energy curves along the approximate bending coordinates, α (a) and β (b), of the transition state calculated by the MRCISD/cc-pVQZ method. A definition of the coordinate is shown on top of each trace. Crosses denote MRCISD energies without Davidson correction. Open circles denote MRCISD+Q energies calculated at MRCISD optimized geometry and solid lines denote their Fourier series regressions.

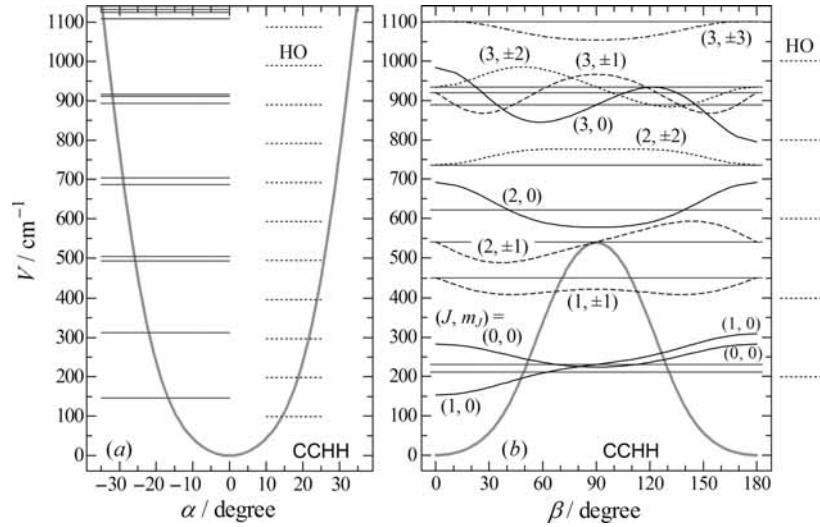

Figure 7. Vibrational energy structures of the degenerate bending modes of the transition state. (a) Energy levels for the α-bending mode of the $^{12}C_2{}^1H_2$ transition state. The harmonic oscillator (HO) energy levels are shown by dotted lines for comparison. (b) Energy levels and wave functions for the β-bending mode of the $^{12}C_2{}^1H_2$ transition state. J and m_J are the rotational quantum number and its projection on to the molecular axis, respectively. Energy levels of HO approximation are shown by dotted lines to the right of the frame.

by expanding the eigenfunctions with the associated Legendre functions by using the BEx1D program.[42] Calculated energy levels for the α-bending mode of CCHH transition state are shown in Figure 7a. The eigenvalues and eigenfunctions for the β-bending motion are shown in Figure 7b. The energy level structure is significantly different from the independent harmonic oscillator assumption with the frequencies 99 and 201 cm^{-1} for α- and β-bending of CCHH, respectively. The partition functions for two bending modes were evaluated directly from the calculated energy levels properly weighted according to the nuclear spin statistics. The TST rate constants calculated by the direct anharmonic treatment for bending motions of TS are plotted by the solid lines in Figure 4. Though the effect was minor, the partition functions for the reactants, H_2/D_2 and $C_2(X)$, were directly calculated from the rovibrational-state energies by using the well-known spectroscopic constants.[37] The nuclear spin statistics were also explicitly taken into account. Similarly to the case of HO model, the potential barrier was slightly adjusted ($\Delta_{adj}E = -1.8$ kJ mol^{-1}) to reproduce the experimental rate constants at around 340 K. Agreement with the experimental rate constants was satisfactory considering the experimental uncertainties.

Discussion

Mechanism of $C_2(X) + H_2$. It has been well-known that the reactions of open singlet species, such as $O(^1D)$, $NH(a^1\Delta)$, and $CH_2(^1A_1)$, with H_2 proceed via an insertion mechanism, initially forming vibrationally excited intermediates (H_2O*, NH_3*, and CH_4*) without significant entrance barriers.[43−45] As discussed by Reisler et al.,[12] if the RHF electron configuration, $(2\sigma_g^+)^2(2\sigma_u^+)^2(1\pi_u)^4$, is assumed for $C_2(X)$, no significant barrier is expected for both perpendicular approach of C_2 to H−H bond (leading to :C═CH_2) and parallel approach of C_2 to H_2 (leading to HC≡CH). However, present MRCISD+Q/aug-cc-pV5Z calculations showed that the TS for perpendicular approach, which is a second-order saddle point corresponding to the β = 90° point in Figure 6b, was found above the collinear TS by 538.5 cm^{-1}, and the TS for parallel approach, corresponding to α = 90° second-order saddle point in Figure 6a was much higher, by 7108.8 cm^{-1} above the collinear TS. These results can be ascribed to the significant contribution of the excited configuration $(2\sigma_g^+)^2(2\sigma_u^+)^0(1\pi_u)^4(3\sigma_g^+)^2$ in the ground electronic state of C_2, and multireference treatment is essentially important for this reaction system. This MCSCF interpretation

is essentially equivalent to the intuitive picture of two-centered singlet biradical (·C≡C·) discussed in the Introduction, which is, though, a GVB (generalized valence bond) or an UHF (unrestricted Hartree−Fock) picture of the electronic state.

Statistical Theory and Kinetic Isotope Effect. The experimental rate constants for both $C_2(X) + H_2$ and $C_2(X) + D_2$ could be well reproduced by transition-state theory when the anharmonicity of the two bending modes of the TS were properly taken into account. The failure of the conventional TST with the harmonic oscillator approximation has been also reported in the previous study on the reactions of OH + benzene and toluene.[29] The anharmonic treatment may be generally important in this category of reactions involving external hydrogen abstraction. It is also interesting to note that the procedure applied for the anharmonic treatment of the TS in this and previous[29] study effectively incorporates the variational effect. For each potential energy calculation along the bending coordinate, a saddle-point optimization is performed. This procedure corresponds to the geometry optimization along the "ridge line" starting from the saddle point, and it cuts out a narrowest cross section of the reaction path. The procedure may require some more computational cost for the saddle-point optimization but can be a more universal method to incorporate both the anharmonicity and the variational effects. In some cases, the reverse may also be true, that is, the anharmonicity of the bending vibrations may be effectively taken into account by the variational treatment.

As discussed in the Introduction, the rate-constant measurements for isotopic reactions with temperature dependence serve as a rigorous test for the statistical theory, and the success of the TST in the present study indicates the validity of the statistical theory even for this small reaction system involving only four atoms. One thing that should be mentioned here is that the energy adjustment from the MRCISD+Q/aug-cc-pV5Z potential energy, $\Delta_{adj}E = -1.8$ kJ mol^{-1}, needed to reproduce the experimental results seems to be large for the error of this level of theory. It may be ascribed to the size inconsistency considering the large effect of the Davidson correction on the potential energy in the vicinity of the transition state, which is located in the very early part of the reaction coordinate. Of course, the error should not be in the energy alone. For example, for the loose anharmonic bending modes, only 20−30% of error in the partition function corresponds to 0.5−0.7 kJ mol^{-1} error in energy in the middle of the present experimental temperature range, 340 K.

Conclusion

Rate constants for the reactions of $C_2(X) + H_2/D_2$ have been measured in the temperature range 293−395 K at a total pressure of 10 Torr (He) by the PLP/LIF method using the Mulliken system of C_2. The results were well reproduced by the TST calculations based on the MRCISD+Q/aug-cc-pV5Z level quantum chemical calculations when the anharmonic bending modes of the transition state were properly treated. The result indicates the validity of the statistical theory for this tetra-atomic system. Anharmonicity of the bending modes of the TS are suggested to be generally important for this class of reaction involving hydrogen abstraction. The Davidson correction was found to be significant for the calculation of the potential energy surface around the early TS.

Acknowledgment. This work was supported by a grant-in-aid by the Ministry of Education, Culture, Sports, Science and Technology of Japan (Grant No. 16750003). We thank professor Y. Endo for providing CPUs for some of the theoretical calculations.

Supporting Information Available: Figure 1S showing laser fluence dependence of the LIF intensity, Figure 2S which is the contour plot of the potential energy surface for the collinear $C_2(X) + H_2$ reaction, Table 1S listing the calculated energy levels of the degenerate two-dimensional bending modes of the TS, and Table 2S and Figure 3S summarizing the partition function calculations for the bending modes of the TS. This material is available free of charge via the Internet at http://pubs.acs.org.

References and Notes

(1) Souza, S. P.; Luts, B. L. *Astrophys. J.* **1977**, *216*, L49.
(2) Fink, U.; Hicks, M. D. *Astrophys. J.* **1996**, *459*, 729.
(3) Grevesse, N.; Sauval, A. J. *Astron. Astrophys.* **1973**, *27*, 29.
(4) Bleekrode, R.; Nieuwpoort, W. C. *J. Chem. Phys.* **1965**, *43*, 3680.
(5) Baronavski, A. P.; McDonald, J. R. *Appl. Opt.* **1977**, *16*, 1897.
(6) Reisler, H.; Mangir, M.; Wittig, C. *J. Chem.Phys.* **1979**, *71*, 2109.
(7) Filseth, S. V.; Hancock, G.; Fournier, J.; Meier, K. *Chem. Phys. Lett.* **1979**, *61*, 288.
(8) Donnelly, V. M.; Pasternack, L. *Chem. Phys.* **1979**, *39*, 427.
(9) Pasternack, L.; McDonald, J. R. *Chem. Phys.* **1979**, *43*, 173.
(10) Reisler, H.; Mangir, M.; Wittig, C. *Chem. Phys.* **1980**, *47*, 49.
(11) Mangir, M. S.; Reisler, H.; Wittig, C. *J. Chem. Phys.* **1980**, *73*, 829.
(12) Reisler, H.; Mangir, M. S.; Wittig, C. *J. Chem. Phys.* **1980**, *73*, 2280.
(13) Pasternack, L.; Baronavski, A. P.; McDonald, J. R. *J. Chem. Phys.* **1980**, *73*, 3508.
(14) Pasternack, L.; Pitts, W. M.; McDonald, J. R. *Chem. Phys.* **1981**, *57*, 19.
(15) Pitts, W. M.; Pasternack, L.; McDonald, J. R. *Chem. Phys.* **1982**, *68*, 417.
(16) Becker, K. H.; Donner, B.; Freitas Dinis, C. M.; Geiger, H.; Schmidt, F.; Wiesen, P. *Z. Phys. Chem.* **2000**, *214*, 503.
(17) Fontijn, A.; Fernandez, A.; Ristanovic, A.; Randall, M. Y.; Jankowiak, J. T. *J. Phys. Chem. A* **2001**, *105*, 3182.
(18) Ristanovic, A.; Fernandez, A.; Fontijn, A. *J. Phys. Chem. A* **2002**, *106*, 8291.
(19) Huang, C.; Zhu, Z.; Xin, Y.; Pei, L.; Chen, C.; Chen, Y. *J. Chem. Phys.* **2004**, *120*, 2225.
(20) Huang, C.; Li, Z.; Zhao, D.; Xin, Y.; Pei, L.; Chen, C.; Chen, Y. *Chin. Sci. Bull.* **2004**, *49*, 438.
(21) Huang, C.; Zhao, D.; Pei, L.; Chen, C.; Chen, Y. *Chem. Phys. Lett.* **2004**, *389*, 230.
(22) Huang, C.; Zhu, Z.; Wang, H.; Pei, L.; Chen, Y. *J. Phys. Chem. A* **2005**, *109*, 3921.
(23) Zhang, X.; Ding, Y.; Li, Z.; Huang, X.; Sun, C. *Chem. Phys. Lett.* **2000**, *330*, 577.
(24) Skell, P. S.; Jackman, L. M.; Ahmed, S.; McKee, M. L.; Shevlin, P. B. *J. Am. Chem. Soc.* **1989**, *111*, 4422.
(25) Hay, P. J.; Hunt, W. J.; Goddard, W. A., III. *J. Am. Chem. Soc.* **1972**, *94*, 8293.
(26) Wolfsberg, M. *Annu. Rev. Phys. Chem.* **1969**, *20*, 449.
(27) Baboul, A. G.; Curtiss, L. A.; Redfern, P. C.; Raghavachari, K. *J. Chem. Phys.* **1999**, *110*, 7650.
(28) (a) Montgomery, J. A., Jr.; Frisch, M. J.; Ochterski, J. W.; Petersson, G. A. *J. Chem. Phys.* **2000**, *112*, 6532. (b) Montogomery, J. A., Jr.; Frisch, M. J.; Ochterski, J. W.; Peterson, G. A. *J. Chem. Phys.* **1999**, *110*, 2822.
(29) Seta, T.; Nakajima, M.; Miyoshi, A. *J. Phys. Chem. A* **2006**, *110*, 5081.
(30) Bauer, W.; Becker, K. H.; Hubrich, C.; Meuser, R.; Wildt, J. *Astrophys. J.* **1985**, *296*, 758.
(31) Douay, M.; Nietmann, R.; Bernath, P. F. *J. Mol. Spectrosc.* **1988**, *131*, 250.
(32) Curtis, L.; Engman, B.; Erman, P. *Phys. Scr.* **1976**, *13*, 270.
(33) Sorkhabi, O.; Xu, D. D.; Blunt, V. M.; Lin, H.; Price, R.; Wrobel, J. D.; Jackson, W. M. *J. Mol. Spectrosc.* **1998**, *188*, 200.
(34) Chase, M. W. NIST-JANAF Thermochemical Tables, 4th ed. *J. Phys. Chem. Ref. Data, Monograph 9*; American Chemical Society: Washington, DC, 1998.
(35) Davis, S. P.; Abrams, M. C.; Phillips, J. G.; Rap, M. L. P. *J. Opt. Soc. Am. B* **1988**, *5*, 2280.
(36) Werner, H.-J.; Knowles, P. J.; Lindh, R.; Manby, F. R.; Schütz, M.; Celani, P.; Korona, T.; Mitrushenkov, A.; Rauhut, G.; Adler, T. B.; Amos, R. D.; Bernhardsson, A.; Berning, A.; Cooper, D. L.; Deegan,

M. J. O.; Dobbyn, A. J.; Eckert, F.; Goll, E.; Hampel, C.; Hetzer, G.; Hrenar, T.; Knizia, G.; Köppl, C.; Liu, Y.; Lloyd, A. W.; Mata, R. A.; May, A. J.; McNicholas, S. J.; Meyer, W.; Mura, M. E.; Nicklass, A.; Palmieri, P.; Pflüger, K.; Pitzer, R.; Reiher, M.; Schumann, U.; Stoll, H.; Stone, A. J.; Tarroni, R.; Thorsteinsson, T.; Wang, M.; Wolf, A. MOLPRO, version 2008.1, a package of ab initio programs; see http://www.molpro.net.

(37) Huber, K. P.; Herzberg, G. Molecular Spectra and Molecular Structure, IV. *Constants of Diatomic Molecules*; Van Nostrand Reinhold: New York, 1979.

(38) Bogey, M.; Demuynck, C.; Destombes, J. L. *Mol. Phys.* **1989**, *66*, 955.

(39) Jacox, M. E. *Vibrational and electronic energy levels of polyatomic transient molecules*; American Chemical Society: Washington, DC, 1994.

(40) Eckart, C. *Phys. Rev.* **1930**, *35*, 1303.

(41) Tokmakov, I. V.; Park, J.; Gheyas, S.; Lin, M. C. *J. Phys. Chem. A* **1999**, *103*, 3636.

(42) Miyoshi, A. BEx1D program available at http://www.frad.t.u-tokyo.ac.jp/~miyoshi/bex1d/.

(43) Ho, T.-S.; Hollebeek, T.; Raditz, H.; Harding, L. B.; Schatz, G. C. *J. Chem. Phys.* **1996**, *105*, 10472, and references therein.

(44) Tezaki, A.; Okada, S.; Matsui, H. *J. Chem. Phys.* **1993**, *98*, 3876.

(45) Hancock, G.; Heal, M. R. *J. Phys. Chem.* **1992**, *96*, 10316, and references therein.

JP904165S